

Modelling camera viewing angle deviation to improve nearshore video monitoring

Clément Bouvier^{a,b,*}, Yann Balouin^a, Bruno Castelle^b, Robert Holman^c

^a BRGM, Univ. Montpellier, France

^b CNRS, UMR 5805 EPOC, Univ. Bordeaux, France

^c CEOAS, Oregon State University, USA

ARTICLE INFO

Keywords:

Coastal management
Video monitoring
Image rectification
Empirical modelling

ABSTRACT

Video monitoring the nearshore can provide high-frequency remotely-sensed optical information from which morphological changes and hydrodynamic data can be derived. Although overlooked in most of the studies, it is acknowledged that camera viewing angles can substantially vary in time for a variety of reasons, reducing consistently data accuracy. This paper aims to identify the primary environmental parameters controlling camera shifts at the video monitoring station of Sète (SE France) and develops an empirical model to routinely reduce these deviations. Our model simulates camera movements with an excellent skill (BSS = 0.87) and shows that camera viewing angles' deviation is primarily controlled by the position of the sun during sunny days, making it predictable. This study opens new perspective to routinely improve camera geometry of video monitoring systems.

1. Introduction

Appropriately monitoring the nearshore is challenging given that morphological changes cover a wide range of spatial and temporal scales (Larson and Kraus, 1994). Traditional topo-bathymetric measurements are not compatible with this wide range of scales, mostly because of the cost and the practical difficulties to survey the nearshore (Lippmann and Smith, 2009), particularly in the surf zone. Instead, video monitoring can provide high-frequency remotely-sensed optical information from which morphological changes and hydrodynamic data can be derived. Shoreline-sandbar geometry as well as rip channel positions have long been measured with reasonable accuracy using video stations (Alexander and Holman, 2004; Almar et al., 2010; Gallop et al., 2011; Holman et al., 2006; Lippmann and Holman, 1989; Ruessink et al., 2009). By combining the video-measured shoreline position and elevation, video-based techniques show also good accuracy in estimating the complete intertidal bathymetry for steep beaches (Aarninkhof et al., 2003; Osorio et al., 2012).

A more recently used product from video monitoring is pixel time series (Holman and Stanley, 2007), which are now commonly exploited in coastal research for diverse purposes. Pixel time series usually consists in a 17-min temporal acquisition of high-frequency (2 Hz) measured pixel intensities providing more information none easily measurable in-situ so far. Recent developments and analysis of these time-series give access to multiple parameters still hard to obtain on the field. Such improvements

concern diverse coastal research applications such as optically measuring the runup (Holland et al., 1995; Holman and Guza, 1984), the wave directional spectrum (Lippmann and Holman, 1991), the longshore currents in the surf zone (Chickadel, 2003), the breaking wave height (Almar et al., 2012) or the nearshore subtidal bathymetry (Holman et al., 2013). These measurement techniques do not require sampling and storage of the entire image but just the pixel intensities at a number of individual locations, or along cross-shore or alongshore transects.

To provide validation of such video data and to further infer time series, each (u, v) pixel coordinate must be transformed into (x, y, z) real world coordinates (Fig. 1a and b). To resolve the equation, one of the most used models is the pinhole model (Faugeras, 1993; Hartley and Zisserman, 2004; Heikkila and Silven, 1997; Holland et al., 1997; Pérez Muñoz et al., 2013), whose calibration is performed by using camera locations (x0, y0, z0), camera intrinsic (details about the sensor, the camera view field and the distortion parameters of the lens) and extrinsic (tilt, roll or azimuth angle) parameters. These last three geometry parameters correspond to the viewing angle of the camera (Fig. 2c) and can be computed by a photogrammetric transformation using a number of ground control points of which the real world coordinates have been accurately measured (Holland et al., 1997).

Although overlooked in most of the studies involving video-derived data, it is acknowledged that camera viewing angles can substantially vary in time for a variety of reasons including thermal and wind effects,

* Corresponding author. BRGM, 1039 Rue de Pinville, 34000, Montpellier, France.

E-mail addresses: clement.bouvier@u-bordeaux.fr, c.bouvier@brgm.fr (C. Bouvier), y.balouin@brgm.fr (Y. Balouin), bruno.castelle@u-bordeaux.fr (B. Castelle), holman@coas.oregonstate.edu (R. Holman).

<https://doi.org/10.1016/j.coastaleng.2019.02.009>

Received 5 July 2018; Received in revised form 6 February 2019; Accepted 13 February 2019

Available online 14 February 2019

0378-3839/ © 2019 Elsevier B.V. All rights reserved.

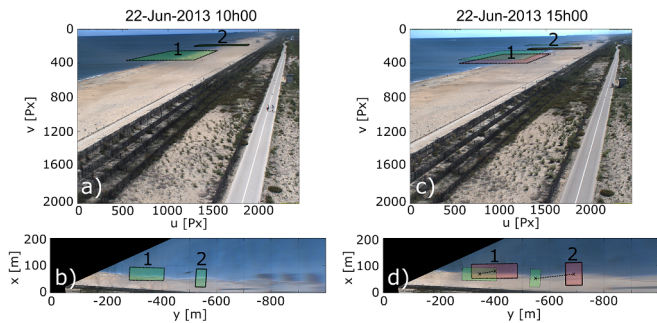


Fig. 1. a) Argus images captured on June 22, 2013 at 10h00 UTC at the beach of Sète (France). b) Associated rectified image with location of two schematic sampling areas (green boxes). Panels c) and d) highlight the impact of camera viewing angle deviation with an image captured a few hours after (at 15h00 UTC) by the same camera.

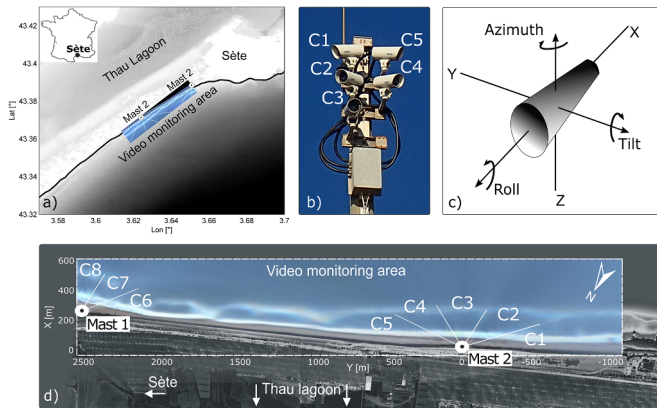


Fig. 2. a) Study site with the location of the video monitoring area. Photography of the video monitoring system deployed at the beach of Sète. Geometry parameters (tilt, roll and azimuth) required for image rectification. Rectified plan view timex images (23 Oct 2011) with indication of the camera fields.

especially on tall towers (Holman and Stanley, 2007). A relatively small shift in tilt and/or roll on camera orientation can lead to shift in a few pixels and, in turn, in real world coordinates on the order meters to tens of meters, or even more depending on the distance of the area of interest from the camera location. Fig. 1a and c provide an extreme example at the video monitoring station of Sète, SE France (Bouvier et al., 2017), with a 0.43° tilt and a 0.15° roll deviation between two images resulting in a large shift in the location, size and shape of the sampling area (colored box on Fig. 1d). This error reaches 130 m in the longshore and 20 m in the cross-shore direction for box 2 located approximately 600 m from the camera.

Such movements are likely to occur for a certain number of outdoor installations (Holman and Stanley, 2007; Pearre and Puleo, 2009; Radermacher et al., 2018; Vousedoukas et al., 2011). Thereby, each image requires a specific geometry solution (tilt, roll and azimuth value) calculated after acquisition assuming camera location and intrinsic parameters remain the same.

An accurate geometry solution for one image is usually obtained detecting a certain number of fixed salient points (ground control points) on the camera fields. Although tedious, this systematic geometry rectification is often efficient in providing accurately rectified images. Consequently, the frequency of accurate geo-rectified images usable for nearshore monitoring often reduce drastically (often more than 90%) depending of the time allowed for the geo-rectification process. Despite attempts to stabilize the camera-mounting structure at certain video monitoring stations (Pearre and Puleo, 2009), camera movement remain significant constraining the user to elaborate a rectification procedure. Previous efforts to

automatically compensate camera movements automatically post-acquisition have been often realized using feature matching (Pearre and Puleo, 2009; Vousedoukas et al., 2011). Such techniques systematically apply a procedure consisting in identifying the deviation of a region of interest, providing the camera viewing angle deviations and then an automatic geo-rectification. Such methods have been further developed with the increased use of drones and became more computationally efficient (Colomina and Molina, 2014; Turner et al., 2016). Such approach can correct high (e.g. induced by the wind) and low frequency (e.g. thermal expansion) camera field movement. However, such a technique requires the presence of fixed salient points (e.g. building, road) or any fixed region with high contrast in the camera view field. If the camera view field essentially consists in the beach and the ocean with no fixed points, which is common in coastal monitoring, camera displacement rectification is not possible and video data are typically taken at face value. The same occurs for scheduled pixel time series acquisitions along a point, a transect or for a grid which can be used, for instance, for depth inversion purposes (Holman et al., 2013). The solution, which would consist in recording each snapshot on which feature matching and geo-rectification would be performed (pending salient fixed points are available), is computationally very expensive and impossible for operational purposes. Therefore, it is crucial to define which environmental variables control the camera movements to further develop generic methods for rectification procedures using time-varying geometry.

This paper aims to identify the primary environmental parameters controlling camera shifts of the Argus station of Sète (SE France) and to propose an empirical model to routinely reduce these deviations after acquisition or even before a scheduled pixel sampling. After a brief description of the video monitoring system of Sète (section 2), the data and method used to unravel the cause of the camera drifts are given in section 3. Results (section 4) are discussed in section 5 before conclusions are drawn in section 6. We show that camera viewing angles deviation is driven by thermal distortion, which make predictable these camera shifts and opens to perspective to routinely improve camera geometry of video monitoring systems.

2. Field site

The Lido of Sète, SE France, is a narrow and relatively straight sandy barrier separating the Thau lagoon from the Mediterranean Sea in the northern part of the Gulf of Lion (Fig. 2a). A large beach management program was developed to mitigate chronic erosion involving the deployment of a 1-km long submerged breakwater. A permanent video monitoring system was installed in April 2011 to study morphological evolution following this coastal management program (Bouvier et al., 2017).

The video monitoring system of Sète consists in 8 cameras mounted on two 20-m high and 2.5-km spaced reinforced concrete mast (Fig. 2d). This study focusses on Mast 2, which provides a complete data time series and offers a 180° view of the beach with 5 cameras (C1 to C5, Fig. 2b) oriented to obtain a panoramic view of the coast (Fig. 2d). Cameras 1 and 5 correspond to longshore oriented cameras with the highest azimuth angle with respect to shore normal ($|Az| > 70^\circ$ in Table 1), while camera 2, 3 and 4 are pointing the sea in a more cross-shore direction ($|Az| < 45^\circ$ in Table 1). Cameras are mounted at different positions and heights on the mast (x_0 , y_0 and z_0 in Table 1); tilt and roll angles are very different depending on cameras orientation.

3. Materials and methods

3.1. Camera geometry data

For approximately 5 years (from April 2011 to April 2016), manual geometry solutions (tilt, roll and azimuth angle) have been determined at the Sète station. Geometry solutions have been tediously obtained using Argus toolbox (Holland et al., 1997) by clicking a certain number of fixed salient points on a large amount of images from each of the 5 cameras.

Table 1

Original geometry parameters for cameras mounted on mast 2 at the station of Sète.

N° Camera	Tilt [°]	Roll [°]	Az [°]	x0 [m]	y0 [m]	z0 [m]
1	78.41	−1.16	79.65	−0.05	0.25	20.42
2	75.20	−2.33	43.90	0.01	0.24	20.10
3	72.87	−3.58	−1.04	0.05	0.31	19.76
4	74.47	1.50	−38.13	−0.01	0.72	20.11
5	80.62	−0.51	−72.27	−0.02	0.75	20.41

Geometry images have been processed approximatively every 15 days and during storms at various times of the day for each camera to extract shoreline/sandbar(s) position for other studies (Balouin et al., 2013; Bouvier et al., 2017). Over 2000 geometry solutions have been computed, that is, approximatively 400 for each camera. The accuracy of such a technique is difficult to generalize but Holman and Stanley (2007) estimated a ± 2 pixel accuracy for a wide-angle camera in a well-managed system. However, considering the large amount of data at Sète and the fact that different operators performed the manual geometry solutions throughout the years, we estimate that the accuracy of our geometry database is approximatively ± 5 pixels. Taking into account the longshore resolution of the system ($dy = 3$ m at 500 m from the mast), we estimate the mean accuracy of the geometry parameters (ΔD) to be approximatively $\pm 0.1^\circ$ for our entire database.

Fig. 3 shows the evolution of the geometry solutions obtained for camera C5. Even if the confidence limit of each solution is within $\pm 0.1^\circ$, large tilt and roll variations (up to 1°) are observed. Only the azimuth angle remains relatively constant and will therefore be considered hereafter as a non-variant geometry parameter. It is important to note that the time variability in geometry parameters can consists in abrupt changes (near august 2015, thick black cross in Fig. 3) due to an occasional update of the basic geometry solution induced during manual intervention on the camera system. Tilt and roll anomalies were computed for each camera by subtracting the average tilt or roll solution (red curve in Fig. 3) until a jump occurs and that a new averaged solution appeared.

Tilt and roll anomaly will be given in degrees as real-world coordinate errors vary spatially. Camera deviations anomaly systematically induces an error in pixels real-world location potentially reaching few hundred meters far from the camera, depending on the grazing angle and lens properties. The induced error (Err) can be approximated using classical trigonometry formulation:

$$\tan(\alpha_{Err}) = \frac{\bar{z}0}{L + Err} - \frac{\bar{z}0}{L}, \quad (1)$$

with α_{Err} ($^\circ$) the camera deviation anomaly, $z0$ (m) the height at which the video system is installed and L (m) the horizontal distance of the

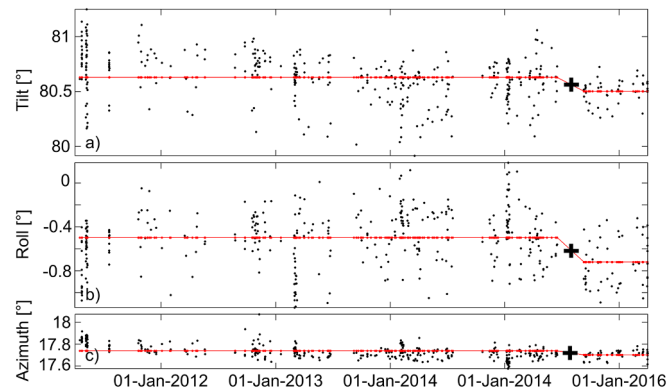


Fig. 3. Time series of geometry solutions for the a) tilt, b) roll and c) azimuth angle of camera C5 at the video monitoring station of Sète. The jump indicated by a black cross corresponds to a slight reset of camera aim. Red line represents the average solution for a non-reset period.

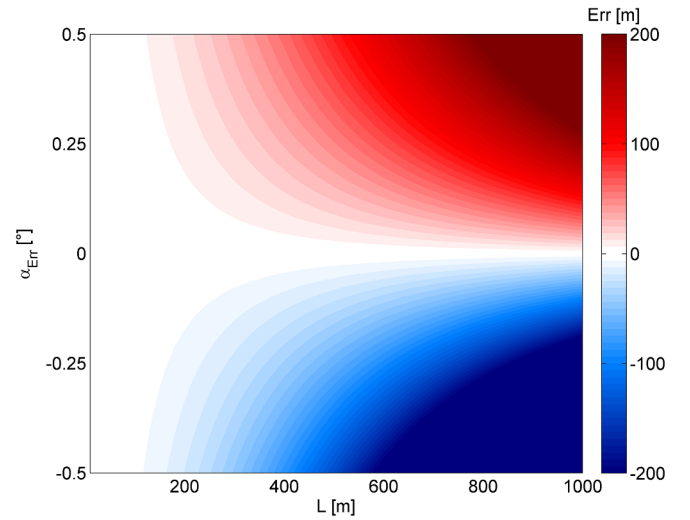


Fig. 4. Estimated geo-rectification errors (Err) depending of the distance from camera to monitored area (L) and of the viewing angle deviation (α_{Err}) for a camera mounted at a 20-m high.

sampling area from the camera. Fig. 4 provides the estimated geo-rectification induced error according to the distance from the camera and camera viewing angle deviation. Depending on camera viewing angle anomaly, the estimated geo-rectification error can reach dramatic values ($Err > 50$ m for $|\alpha_{Err}| > 0.25^\circ$) when the camera is located approximately 200 m from the sampling area, which is a common video monitoring distance.

3.2. Environmental condition

3.2.1. Meteorological data

Specific environmental conditions are assumed to control changes in camera orientation. To verify this hypothesis air temperature (T_{meteo}) and wind condition (velocity and direction) measured every hour by a Meteo France station located a few kilometers away from the video station were collected. The 5-year time series of the longshore and cross-shore wind components (V_l and V_c respectively) were computed hourly. Nebulosity (N_{meteo}) which is a proxy of the percentage of the cloud cover was observed every 3 h as an integer variable 0 (no cloud) to 8 (cloudy). An observer assessed the description of the state of the sky according to the criteria most frequently adopted. Nebulosity is then linearly interpolated every hour. Using these parameters, each camera geometry data (tilt and roll) was linked to a set of environmental data.

3.2.2. Solar position

Structure deformation can occur as a result of thermal dilatation caused by solar absorption (Assem, 2011). To assess these effects, solar position was used as a proxy of solar absorption as it indicates the exact position of the sun (Fig. 5). Solar azimuth and elevation angle (ϕ_s and α_s respectively) were computed for each camera geometry data according to (Reda and Andreas, 2004):

$$\phi_s = \text{Arctan2}\left(\frac{\sin H'}{\cos H' \cdot \sin \varnothing - \tan \delta' \cdot \cos \varnothing}\right), \quad (2)$$

$$\alpha_s = 90 - \varnothing, \quad (3)$$

with the local hour angle (H'), sun declination (δ') and zenith angle \varnothing observed from a particular point on the Earth surface (here the head of the pole where cameras are mounted). The date and the local coordinates (longitude, latitude and elevation) are needed. Solar azimuth angle varies from -180° to 180° , and is negative and positive when the sun is located eastward and westward, respectively. As is, the sun rises approximatively to the east ($\phi \sim -90^\circ$) and sets to the west ($\phi \sim +90^\circ$)

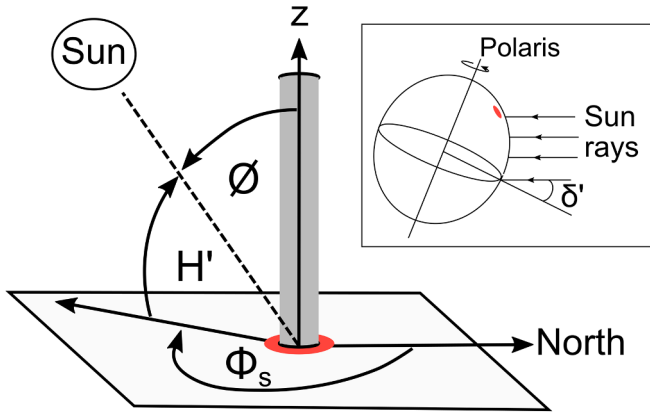


Fig. 5. The position of the Sun in the sky is a function of both the time and the geographic location of observation on Earth's surface.

passing through the south ($\phi = 0^\circ$). The solar elevation angle is the altitude of the sun, that is, the angle between the horizon and the center of the sun's disc.

3.3. Camera deviation models

3.3.1. Models construction

Given that camera geometry data is highly variable in time, identifying the preferred timescale(s) of geometry changes is complex. Despite the extensive data set used for training, the application of Artificial Neuronal Network (ANNs) was disregarded. The two primary reasons are that ANNs hamper the physical interpretation of the results and they typically provide unreliable prediction beyond the range represented by the training dataset. Robust methods such as based on Principal Component Analysis were also disregarded as they would lead to the loss of any cause-effect relationship between each variable. On the contrary, a 3rd degree polynomial regression model provides a unique value of regression coefficients, a moderate flexibility of shape, interpretable results and makes possible interactions between dependent variables. Such models were computed with multiple explanatory parameters (see eqs. (4) and (5) below) and processed separately as a function of the observed camera tilt and roll angle deviation (T_{ObsAz} and R_{ObsAz} respectively). $F1_{az}$ and $F2_{az}$ correspond to the tilt and roll polynomial regression equations with $\epsilon1_{az}$ and $\epsilon2_{az}$ the associated error of the least square method. The index Az indicates the average azimuth angle of each camera with respect to shore normal:

$$T_{ObsAz} = F1_{az}(\phi_s, \alpha_s, T_{meteo}, N_{meteo}, V_c, V_l) + \epsilon1_{az}, \quad (4)$$

$$R_{ObsAz} = F2_{az}(\phi_s, \alpha_s, T_{meteo}, N_{meteo}, V_c, V_l) + \epsilon2_{az} \quad (5)$$

To objectively assess model skill, linear squared-correlation (R^2) and root mean square error (RMSE) between the observed (T_{ObsAz} or R_{ObsAz}) and simulated (T_{SimAz} or R_{SimAz}) camera deviations have been computed. Then to consider measurement error (ΔD in section 3.1), the Brier Skill Score (BSS) has been computed for each model according to (Davidson et al., 2013).

$$BSS = 1 - \frac{\sum ||D_{ObsAz} - D_{SimAz}| - \Delta D|^2}{\sum (D_{ObsAz} - Db)^2}, \quad (6)$$

with D_{ObsAz} and D_{SimAz} the angle deviation observed and simulated respectively. This method compares the model residuals with a suitable baseline (Db). The choice of baseline has been fixed to zero as the variable measured is an anomaly. Positive BSS indicates a significant improvement relative to the base line with a value in excess of 0.0, 0.3, 0.6, 0.8 typically described respectively as 'poor', 'fair', 'good' and 'excellent' (Davidson et al., 2013).

3.3.2. Models' application and sensitivity

To assess the performance of our method, tilt and roll models have been run for camera C1 (second worst model skill; see section 4.1) throughout the 22nd of June 2013 (hindcast) and during a one-year non-trained period starting on April 2016 (forecast). During that period, tilt and roll simulations were compared with more than 50 manually computed geometry solutions (more details in section 3.1).

Finally, in order to determine equations' sensitivity on each of the 6 explanatory variables ($F1_{az}$ and $F2_{az}$), each model has been processed on most possible cases. To reduce the computational time, each variable has been decomposed into (10 by 1) vectors, resulting in 10^5 simulations for one variable tested. Each vector boundary was defined by the percentile 10 and 90 of the variable intensity observed along the study period. Model sensitivity was estimated for each equation $F1_{az}$ and $F2_{az}$ separately by averaging the absolute value of the simulated tilt and roll anomaly along the dynamic variable.

4. Results

4.1. Models performance

Fig. 6 shows the fit of the tilt and roll anomaly models for each of the 5 cameras (T_{ObsAz} and R_{ObsAz} versus T_{SimAz} and R_{SimAz}). Camera viewing angle deviation models were found to significantly reproduce the tilt and roll variability along the study period (from April 2011 to April 2016). Brier Skill Score (BSS) indicates that models were rated as 'excellent' (BSS = 0.87). Root mean square error (RMSE) is relatively small compared to the range of variations simulated ($\approx 60\%$ of the observed tilt and roll anomalies is greater than the 0.12° RMSE). Furthermore, RMSE remains slightly higher than the estimated $\pm 0.1^\circ$ geometry accuracy (dashed lines in Fig. 6) which suggests a good performance of the polynomial regression models. Coefficient of determination (R^2) reveals that our method explains on average 71% of the camera viewing angle deviation variability.

Details of the polynomial regression are provided for each models in Table 2. Statistical measurement of the tilt and roll models have been realized for each camera separately. Results indicate that model quality remains homogenous except for the roll anomaly on camera 5 ($F2_{72}$). Even if BSS score is relatively high (0.74), the coefficient of

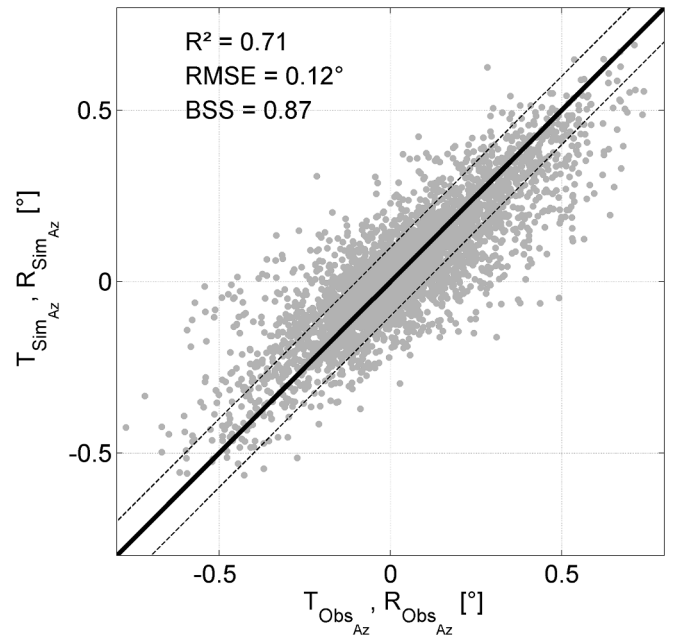


Fig. 6. Model predictions (T_{SimAz} and R_{SimAz}) versus observations (T_{ObsAz} and R_{ObsAz}). The solid line is the linear function $f(x) = y$. Dashed lines represent the estimated geometry accuracy interval $f(x) = y \pm 0.1$.

Table 2
Results of the 3rd degree polynomial regression models.

N° Camera	$F1_{az}$			$F2_{az}$		
	R^2	RMSE [°]	BSS	R^2	RMSE [°]	BSS
C1 (az = 80°)	0.74	0.08	0.84	0.61	0.12	0.84
C2 (az = 44°)	0.80	0.07	0.86	0.78	0.11	0.90
C3 (az = -1°)	0.77	0.09	0.88	0.76	0.12	0.92
C4 (az = -38°)	0.84	0.08	0.90	0.66	0.14	0.88
C5 (az = -72°)	0.77	0.10	0.91	0.38	0.19	0.74

determination (R^2) is weak and RMSE remains high (0.19°). It is suspected that the inaccuracy of the $F2_{-72}$ model is highly related to the quality of the roll angle observations. Roll angle was relatively difficult to obtain precisely for this camera because of the practical difficulty to identify ground control points resulting in errors on the roll anomaly values and the inaccuracy of the $F2_{-72}$ model.

4.2. Model application

To assess the performance of our method, tilt and roll models have been run throughout the 22nd of June 2013 and during a one-year non-trained period starting on April 2016. We choose for this test the second worst model skill ($F1_{80}$ and $F2_{80}$) used to reproduce the camera C1 variability (see Table 2).

4.2.1. One-day application

The 22nd of June 2013 has been presented in the introduction as a day with high camera tilt and roll variability (Fig. 1). Inputs of the model are presented in Fig. 7a, b and c. Elevation and azimuth angle of the sun varied respectively from 0 to 70° and -150 to 150° during the day. Nebulosity was very low (no clouds) and remained nearly the same while air temperature slightly increased until 15h00 UTC. The coast was exposed to a reasonably constant offshore wind from NW during the entire day (-3.83 m/s and -1.44 m/s on average for the cross-shore and longshore component respectively).

Tilt and roll anomaly varied approximately from -0.2° to 0.4° (Fig. 7d and e). Even if direct correlation with model inputs (Fig. 7a–c) is readily difficult to identify, both models reproduce the observed camera viewing angle anomaly with fair accuracy. Considering the estimated geometry accuracy, root mean square error is low (RMSE < 0.1°) and coefficient of determination is good ($R^2 > 0.76$) for both models. We suspect that the deviations from the observed roll anomaly could be due to an inaccurate ground control point manual detection when processing the camera geometry (R_{Obs80} in Fig. 7e).

4.2.2. One-year application

Even if the first objective of the model presented was primarily more to better identify the primary environmental parameters controlling camera shifts, a comparison between manually resolved camera viewing angle deviations and model estimations is given Fig. 8. The model was applied to a one-year non-trained period for camera 1 providing the estimated camera viewing angle deviation. The comparison between observed and simulated tilt and roll anomalies (Fig. 8d and e) shows less accuracy than in Fig. 7 with a root-mean square error reaching 0.15° in roll anomaly. However, solutions determined by the model significantly reduces the camera viewing angle anomaly and shows a good skill in prediction (BSS > 0.8). A conversion of the angle anomaly (°) into a real-coordinate error (m) provides additional into model improvement. For a 20-m high positioned camera, a 0.4° improvement of the camera viewing angle anomaly leads to a 100 m error correction in pixel position at a distance of 500 m from the camera (Fig. 4).

4.3. Model sensitivity

To determine model sensitivity to each variable, each model has

been run on all possible cases (section 3.3.2). The evolution of the simulated averaged absolute deviations ($|T_{SimAz}|$ and $|R_{SimAz}|$) are presented in Fig. 9 for each model (different colors) as a function of variable evolution (different panels). When varying the solar azimuth angle or the nebulosity, the averaged deviation anomalies were strongly affected for all models (Fig. 9a and c). These results suggest an important sensitivity of all models to both variables. The value of the camera viewing angle deviation anomaly shows a dependency to the solar azimuth angle (ϕ_s) depending on camera orientation (λ_z) on the mast (Fig. 9a). Moreover, with low nebulosity (no clouds), we observe a large averaged deviation value for all models, and the contrary with intense nebulosity (Fig. 9c). It is therefore deduced that low cloud cover is important to observe large tilt and roll variation. This behavior suggests that camera viewing angle deviations were linked to the deformation of the mast by solar absorption, which will be discussed in section 5. In contrast, the simulated deviations were less affected when varying other environmental parameters (Fig. 9b, d, e, f).

To quantify the influence of each variable for all models, standard deviation of these curves have been computed. Results were averaged over all models and finally normalized across each variable. This parameter is presented as a sensitivity index (S_{var}) in Table 3. Even if wind forcing is sometimes blamed for being responsible for camera deviation (Rutten et al., 2017; Voudoukas et al., 2011), in the case of Sète, model sensitivity to longshore or cross-shore wind components remains very low ($S_{var} < 0.2$ for both variables in Table 3). Air temperature and solar elevation angle do not affect significantly camera deviations neither with a S_{var} of 0.1 and 0.16, respectively.

5. Discussion

Until recently, camera movements in fixed platform imagery for coastal application were largely ignored. Holman and Stanley (2007) introduced this difficulty highlighting that camera viewing angles regularly shift slightly for a variety of reasons including primarily thermal and wind effects, especially on tall towers. At the video monitoring system of Duck, North Carolina, camera viewing angle deviations can be described as a diurnal signal of about 2-pixel range, resulting in an approximately 30-m longshore drift, 1 000 m away from the camera according to the pixel resolution of the video station. These deviations were only observed during sunny days, similar to our observations at Sète. Pear and Puleo (2009) also reported deviations of the video monitoring system at Rehoboth Beach, Delaware leading to important errors on the plan view image (estimated 500-m shift 2 300 m from the camera). Similarly, Voudoukas et al. (2011) observed cameras movement at the video system of Algarve, South Portugal introducing significant geo-rectification errors.

Each time, the automatic correction methods consisted in determining the cameras viewing angle deviation using a template matching method. Small, high-contrast regions (templates) from an original base image are matched against corresponding locations in subsequent images, providing the missing pinhole model extrinsic parameters (tilt, roll and azimuth). Such a technique requires a region of interest selection in the camera view field consisting of fixed objects with distinct contrast. However, for many coastal areas, this kind of pattern is not easily identified from camera images. Moreover, for scheduled pixel time series acquisitions, users need to anticipate the camera shift to produce a well-referenced pixel acquisition. Camera movements will not only induce the displacement of the area sampled, but also a modification of the acquired pixel grid resolution. If not corrected, significant errors are introduced when analyzing remotely-sensed hydrodynamic data such as longshore currents, run-up or wave celerity. At the Sand Motor, a mega-scale beach nourishment in the Netherlands, Radermacher et al. (2018) observed important errors in the remotely-sensed bathymetry depending on camera gaze angles.

Therefore, it is crucial to define which environmental variables control those camera movements in order to minimize these deviations

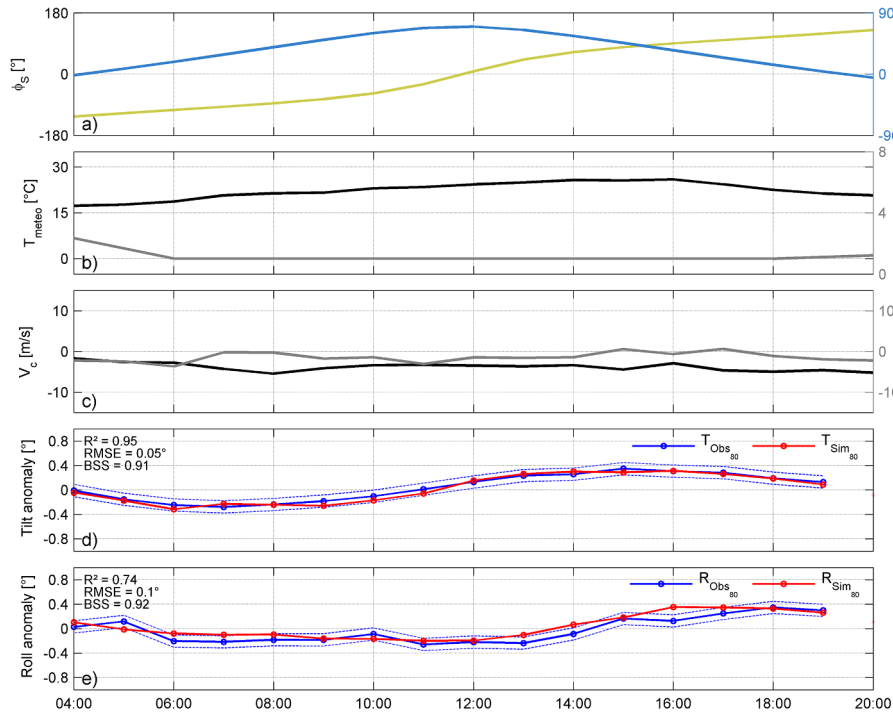


Fig. 7. Tilt and roll anomaly forecast for camera 1 during the 22nd of June 2013. Panels a), b) and c) present the model inputs with respectively, the position of the sun (ϕ_s , α_s), weather condition (T_{meteo} , N_{meteo}) and wind velocity (V_c , V_l). Panels d) and e) illustrate tilt and roll anomaly outputs (pinkish red dots) and also provide a comparison between modeled (red dots on thick curve) and observed (blue dots on thick curve) camera viewing angle deviation.

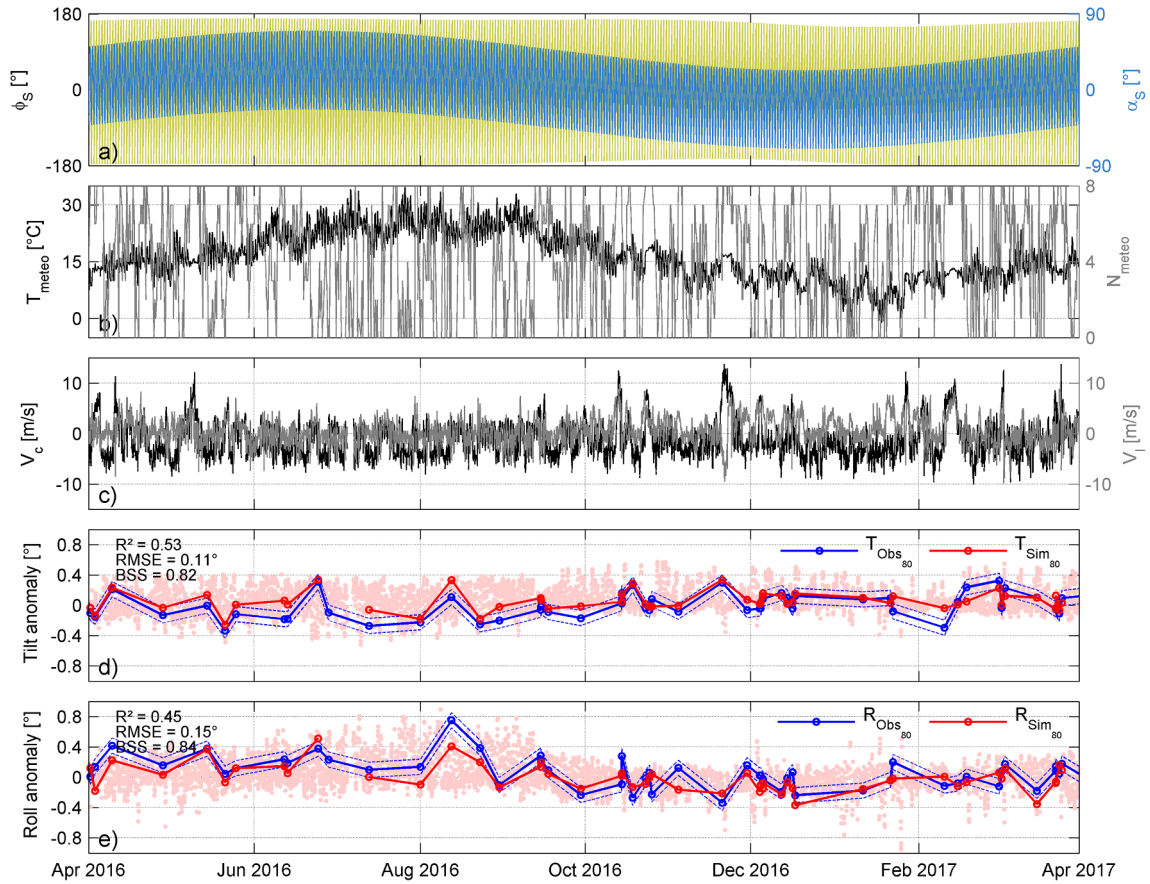


Fig. 8. Tilt and roll anomaly forecast for camera 1 during a one year period from April 2016. Panels a), b) and c) present the model inputs with respectively, the position of the sun (ϕ_s , α_s), weather condition (T_{meteo} , N_{meteo}) and wind velocity (V_c , V_l). Panels d) and e) illustrate tilt and roll anomaly outputs (pinkish red dots) and also provide a comparison between modeled (red dots on thick curve) and observed (blue dots on thick curve) camera viewing angle deviation.

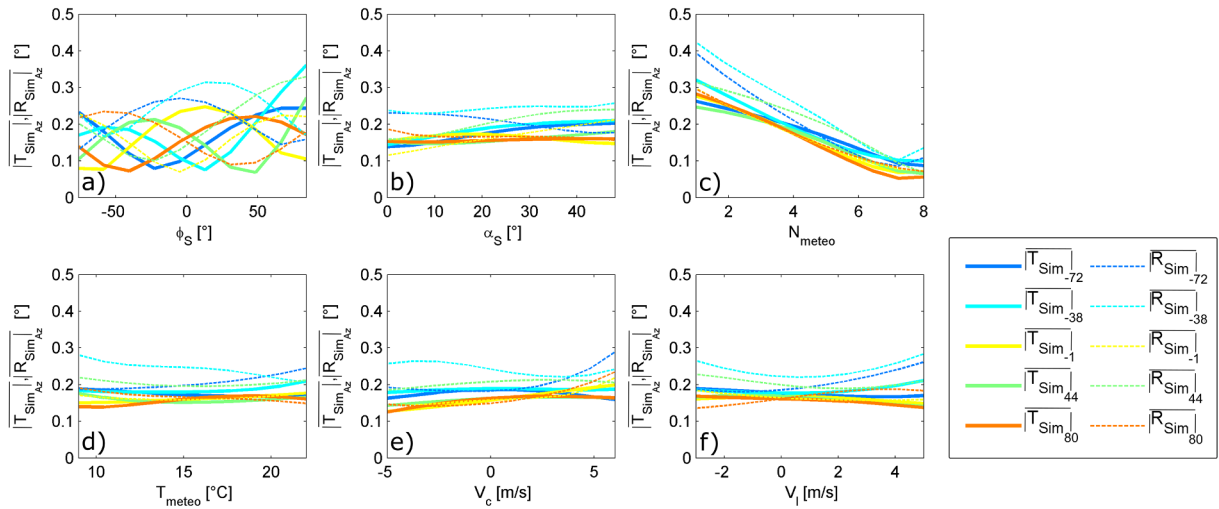


Fig. 9. a) to f) Model sensitivity to each variable. Simulated averaged absolute tilt (T_{SimAz}) and roll (R_{SimAz}) deviation computed along each environmental variable (different panel) and presented for each model (different colors).

Table 3

Model sensitivity index S_{Var} to all environmental variables.

Variable	ϕ_s	α_s	N_{meteo}	T_{meteo}	V_c	V_l
S_{Var}	0.58	0.16	0.76	0.10	0.16	0.13

for futures video system deployment. This will also help designing appropriate data collection plan for which no deviation is suspected, which opens new perspectives to develop generic methods for rectification procedures using time-varying geometry (Bergsma et al., 2014). While the robustness of the polynomial regression inputs was questionable (not only measurement accuracy but also the choice to simulate camera deviations as an instantaneous response to environmental forcing), high skill was found for all models. Sensitivity analysis highlighted that all models are primarily controlled by the solar azimuth angle and the nebulosity. While low cloud cover has been clearly identified to systematically affect camera movements, processes connecting camera shifts with solar azimuth angle remains misunderstood.

To fully understand which processes induce camera deviations, tilt and roll anomaly simulations (Fig. 10a and b respectively) are presented as a function of solar azimuth angle (ϕ_s) for each camera orientation (Az) while others variables have been fixed (see the legend in Fig. 10). The maximum anomaly for C5 up to C1 occurs for progressively increasing solar azimuth angle. It is important to note that cameras C1 and C5, which are looking towards opposite direction (ENE and WSW, respectively), show very similar but out of phase deviations. Moreover, tilt and roll deviations patterns are clearly connected. For instance, a tilt deviation on a southward-looking camera (C3), is related with a roll deviation on an eastward- or westward-looking camera (C1 and C5). These results

show that camera deviations are controlled by a local thermal deformation of the pole on which they are mounted. This process is induced by solar absorption of the face of the structure exposed to the sun leading to its dilatation. From structural mechanics, it is well known that temperature gradient across any cross section of a determined element (in this case the mast) produces changes of its curvature (Kassimali and Garcilazo, 2010). According to the theory, the mast will arc in the same direction of the temperature gradient, here from the enlighten face of the mast toward the opposite side. Instead of empirically modelling camera movements as if they were independent, one solution could be to determine directly the deformation of the pole where the camera are mounted depending of the environmental parameters, providing the camera viewing angle deviation for each camera. Technically, the solution is powerful but difficult to implement as it is highly influenced by the shape of the structure and the specific camera mount.

A major advantage of the model described in this study is to assess a complete time series of such camera movements at high frequency. While one specific day has been highlighted (section 4.2.1), model outputs also showed a certain seasonality. Lower anomalies amplitude is generally observed during the winter period (pinkish red dots in Fig. 8d and e). This behavior could be explained by the cloud cover, generally higher in winter, which reduces sun action on the pole, resulting in lower changes in camera viewing angle. Although the model described in this study reproduced correctly the camera viewing angle deviation observed at Sète during the last 5 years, some errors on the prediction can occur when the environmental input data is not (or poorly) represented (very low temperature, high wind forces) during the model construction phase (polynomial regression). It is therefore anticipated that model skill increases with increasing amount, quality and range of training environmental data.

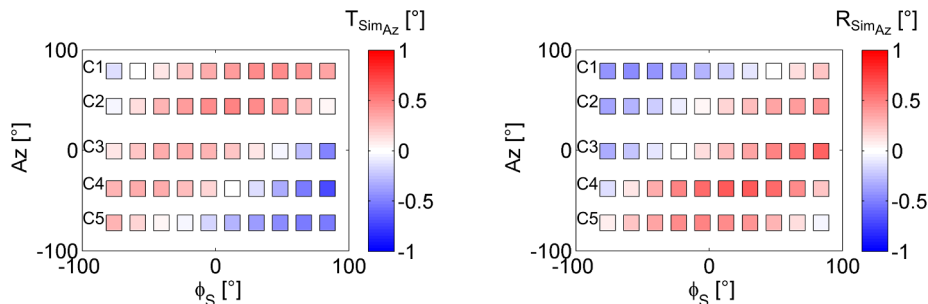


Fig. 10. Simulation of the tilt and roll anomaly (T_{SimAz} , R_{SimAz} in a) and b), respectively) as a function of solar and camera azimuth angle (ϕ_s and Az respectively). For each simulation, nebulosity has been set to 1, solar elevation angle to 21°, temperature to 15 °C and cross-shore/longshore wind component to 0 m/s.

6. Conclusion

We showed that camera viewing angle deviations can induce large errors, with for instance more than 200 m and 20 m during a day in the longshore and cross-shore direction, respectively, at the video monitoring station of Sète. This correction remains sometimes difficult for seaward-looking camera and pixel time series because of the practical difficulty to identify ground control points. At the video monitoring station of Sète, cameras viewing angle deviations are controlled by thermal deformation of the pole where they are mounted. Deviation magnitude depends mainly on cloud cover, with a daily evolution due to camera orientation and solar azimuth angle. These deviations have been simulated using a polynomial regression method with good accuracy allowing a significant reduction of the geo-rectification errors. This method is applicable to other field sites subject to camera viewing angle anomaly. This study opens new perspectives in video monitoring, particularly to routinely improve camera geometry of video monitoring systems and to further derive higher quality remotely sensed hydrodynamic and morphological products.

Acknowledgements

The video system used in this work was funded by Thau Agglo and BRGM. CB acknowledges financial support from BRGM through a PhD grant. BC is funded by CHIPO (grant number ANR-14-ASTR-0004-01) supported by the Agence Nationale de la Recherche (ANR). L. Desbiendras, J. Tesson, R. Belon, M. Giusti, Y. Colombet, P.-A. Picand, F. Longueville, A. Latapy, S. Hureau and M. Guebba are greatly acknowledged for their help in processing video data.

References

- Aarninkhof, S.G.J., Turner, I.L., Dronkers, T.D.T., Caljouw, M., Nipius, L., 2003. A video-based technique for mapping intertidal beach bathymetry. *Coast. Eng.* [https://doi.org/10.1016/S0378-3839\(03\)00064-4](https://doi.org/10.1016/S0378-3839(03)00064-4).
- Alexander, P.S., Holman, R.A., 2004. Quantification of nearshore morphology based on video imaging. *Mar. Geol.* 208, 101–111. <https://doi.org/10.1016/j.margeo.2004.04.017>.
- Almar, R., Castelle, B., Ruessink, B.G., Sénéchal, N., Bonneton, P., Marieu, V., 2010. Two- and three-dimensional double-sandbar system behaviour under intense wave forcing and a meso-macro tidal range. *Cont. Shelf Res.* <https://doi.org/10.1016/j.csr.2010.02.001>.
- Almar, R., Cienfuegos, R., Catalán, P.A., Michallet, H., Castelle, B., Bonneton, P., Marieu, V., 2012. A new breaking wave height direct estimator from video imagery. *Coast. Eng.* 61, 42–48. <https://doi.org/10.1016/j.coastaleng.2011.12.004>.
- Assem, E.O., 2011. Correlating thermal transmittance limits of walls and roofs to orientation and solar absorption. *Energy Build.* 43, 3173–3180. <https://doi.org/10.1016/j.enbuild.2011.08.015>.
- Balouin, Y., Tesson, J., Gervais, M., 2013. Cuspate shoreline relationship with nearshore bar dynamics during storm events – field observations at Sète beach, France. *J. Coast Res.* 65, 440–445. <https://doi.org/10.2112/SI65-075.1>.
- Bergsma, E.W.J., Conley, D.C., Davidson, M.A., O'Hare, T.J., Holman, R.A., 2014. An assessment of video-based bathymetry estimation in a macro-tidal environment. *Coast. Eng. Proc. 34th Conf. Coast. Eng.* 1–10.
- Bouvier, C., Balouin, Y., Castelle, B., 2017. Video monitoring of sandbar-shoreline response to an offshore submerged structure at a microtidal beach. *Geomorphology* 295, 297–305. <https://doi.org/10.1016/j.geomorph.2017.07.017>.
- Chickadel, C.C., 2003. An optical technique for the measurement of longshore currents. *J. Geophys. Res.* 108, 3364. <https://doi.org/10.1029/2003JC001774>.
- Colomina, I., Molina, P., 2014. Unmanned aerial systems for photogrammetry and remote sensing: a review. *ISPRS J. Photogrammetry Remote Sens.* 92, 79–97.
- Davidson, M.A., Splinter, K.D., Turner, I.L., 2013. A simple equilibrium model for predicting shoreline change. *Coast. Eng.* 73, 191–202. <https://doi.org/10.1016/j.coastaleng.2012.11.002>.
- Faugeras, O., 1993. Three-dimensional Computer Vision: a Geometric Viewpoint. MIT PRESS, Cambridge, Massachusetts. https://doi.org/10.1007/978-3-642-82429-6_2.
- Gallop, S.L., Bryan, K.R., Coco, G., Stephens, S.A., 2011. Storm-driven changes in rip channel patterns on an embayed beach. *Geomorphology* 127, 179–188. <https://doi.org/10.1016/j.geomorph.2010.12.014>.
- Hartley, R., Zisserman, A., 2004. Multiple View Geometry in Computer Vision, second ed. Cambridge UK Cambridge Univ Press.
- Heikkilä, J., Silven, O., 1997. A four step camera calibration procedure within implicit image correction. *Comput. Vis. Pattern recognition, proceedings. IEEE Comput. Soc. Conf.* 1106–1112 1997.
- Holland, K.T., Holman, R. a, Lippmann, T.C., Stanley, J., Plant, N., 1997. Practical use of video imagery in nearshore oceanographic field studies - oceanic engineering. *IEEE Journal of. IEEE J. Ocean. Eng.* 22, 81–92.
- Holland, K.T., Raubenheimer, B., Guza, R.T., Holman, R.A., 1995. Runup kinematics on a natural beach. *J. Geophys. Res.* 100, 4985. <https://doi.org/10.1029/94JC02664>.
- Holman, R., Plant, N., Holland, T., 2013. CBathy: a robust algorithm for estimating nearshore bathymetry. *J. Geophys. Res. Ocean.* <https://doi.org/10.1002/jgrc.20199>.
- Holman, R.A., Guza, R.T., 1984. Measuring run-up on a natural beach. *Coast. Eng.* 8, 129–140. [https://doi.org/10.1016/0378-3839\(84\)90008-5](https://doi.org/10.1016/0378-3839(84)90008-5).
- Holman, R.A., Stanley, J., 2007. The history and technical capabilities of Argus. *Coast. Eng.* <https://doi.org/10.1016/j.coastaleng.2007.01.003>.
- Holman, R.A., Symonds, G., Thornton, E.B., Ranasinghe, R., 2006. Rip spacing and persistence on an embayed beach. *J. Geophys. Res. Ocean.* 111, 1–17. <https://doi.org/10.1029/2005JC002965>.
- Kassimali, A., Garcilazo, J.J., 2010. Geometrically nonlinear analysis of plane frames subjected to temperature changes. *J. Struct. Eng.* 136, 1342–1349. [https://doi.org/10.1061/\(ASCE\)ST.1943-541X.0000233](https://doi.org/10.1061/(ASCE)ST.1943-541X.0000233).
- Larson, M., Kraus, N.C., 1994. Temporal and spatial scales of beach profile change, Duck, North Carolina. *Mar. Geol.* 117, 75–94. [https://doi.org/10.1016/0025-3227\(94\)90007-8](https://doi.org/10.1016/0025-3227(94)90007-8).
- Lippmann, T.C., Holman, R.A., 1991. Phase speed and angle of breaking waves measured with video techniques. In: *Coastal Sediments*, pp. 542–556 1991.
- Lippmann, T.C., Holman, R.A., 1989. Quantification of sand bar morphology: a video technique based on wave dissipation. *J. Geophys. Res.* 94, 995. <https://doi.org/10.1029/JC094iC01p0995>.
- Lippmann, T.C., Smith, G.M., 2009. Shallow surveying in hazardous waters. *US Hydrogr. Conf.* 1–12 2009.
- Osorio, A.F., Medina, R., Gonzalez, M., 2012. An algorithm for the measurement of shoreline and intertidal beach profiles using video imagery. *PSDM. Comput. Geosci.* 46, 196–207. <https://doi.org/10.1016/j.cageo.2011.12.008>.
- Pearre, N.S., Puleo, J.A., 2009. Quantifying seasonal shoreline variability at Rehoboth beach, Delaware, using automated imaging techniques. *J. Coast Res.* 254, 900–914. <https://doi.org/10.2112/08-1029.1>.
- Pérez Muñoz, J.C., Ortiz Alarcón, C.A., Osorio, A.F., Mejía, C.E., Medina, R., 2013. Environmental applications of camera images calibrated by means of the Levenberg-Marquardt method. *Comput. Geosci.* 51, 74–82. <https://doi.org/10.1016/j.cageo.2012.07.016>.
- Radermacher, M., de Schipper, M.A., Reniers, A.J.H.M., 2018. Sensitivity of rip current forecasts to errors in remotely-sensed bathymetry. *Coast. Eng.* 135, 66–76. <https://doi.org/10.1016/j.coastaleng.2018.01.007>.
- Reda, I., Andreas, A., 2004. Solar position algorithm for solar radiation applications. *Sol. Energy* 76, 577–589. <https://doi.org/10.1016/j.solener.2003.12.003>.
- Ruessink, B.G., Pape, L., Turner, I.L., 2009. Daily to interannual cross-shore sandbar migration: observations from a multiple sandbar system. *Cont. Shelf Res.* <https://doi.org/10.1016/j.csr.2009.05.011>.
- Rutten, J., Ruessink, B.G., Price, T.D., 2017. Observations on sandbar behaviour along a man-made curved coast. *EARTH Surf. Process. LANDFORMS Earth Surf. Process.* <https://doi.org/10.1002/esp.4158>.
- Turner, I.L., Harley, M.D., Drummond, C.D., 2016. UAVs for coastal surveying. *Coast. Eng.* 114, 19–24. <https://doi.org/10.1016/j.coastaleng.2016.03.011>.
- Vousdoukas, M.I., Ferreira, P.M., Almeida, L.P., Dodet, G., Psaros, F., Andriolo, U., Taborda, R., Silva, A.N., Ruano, A., Ferreira, Ó.M., 2011. Performance of intertidal topography video monitoring of a meso-tidal reflective beach in South Portugal. *Ocean Dynam.* 61, 1521–1540. <https://doi.org/10.1007/s10236-011-0440-5>.